

Article

Influence of Particle Size of CeO₂ Nanospheres Encapsulated in SBA-15 Mesopores on SO₂ Tolerance during NH₃-SCR Reaction

Xinyu Han^{1,2,3} , Mengyao Bian^{1,2,3}, Kaijie Liu^{1,2,3,*}, Xin Yang^{1,2,3}, Daying Zheng^{1,2,3}, Xiangguang Yang^{1,2,3,4} and Yibo Zhang^{1,2,3,4,*} 

¹ Ganjiang Innovation Academy, Chinese Academy of Sciences, No.1, Science Academy Road, Ganzhou 341000, China; xinyuhan@mail.ustc.edu.cn (X.H.); mybian20@gia.cas.cn (M.B.); yxupupup@mail.ustc.edu.cn (X.Y.); dayingz@mail.ustc.edu.cn (D.Z.); xgyang@gia.cas.cn (X.Y.)

² School of Rare Earths, University of Science and Technology of China, Hefei 230041, China

³ Key Laboratory of Rare Earths, Chinese Academy of Sciences, Ganzhou 341000, China

⁴ Changchun Institute of Applied Chemistry, Chinese Academy of Sciences, Changchun 130022, China

* Correspondence: liukaijie@gia.cas.cn (K.L.); yibo Zhang@gia.cas.cn (Y.Z.); Tel.: +86-0797-2130675 (Y.Z.)

Abstract: Ce-based selective catalytic reductions with an NH₃ (NH₃-SCR) catalyst have emerged as a focal point in denitrification catalyst research. However, the correlation between the structural characteristics of Ce-based catalysts and the influence of CeO₂ nanoparticle size on SO₂ resistance remains unclear. CeO₂ nanospheres with different sizes of less than 10 nm were synthesized, and a series of supported CeO₂/SBA-15 catalysts were prepared according to the 10 nm pore size of SBA-15. These catalysts were used to explore the influence of the size of the CeO₂ nanospheres on these catalysts, specifically on their SO₂ resistance in NH₃-SCR reactions. With the increase in size, their SO₂ resistance became stronger. The results of NH₃-TPD, H₂-TPR, and XPS indicated that the catalyst with the largest particle size had the lowest adsorption of SO₂, which was attributed to more acid sites and a mutual effect between Si and Ce, resulting in the best SO₂ resistance. It was also observed that there was less sulfate deposition on the catalyst by thermogravimetric analysis. In situ DRIFTS revealed that after SO₂ poisoning, the NH₃-SCR reaction on the catalyst predominantly follows the E-R mechanism. This study offers recommendations for the development of Ce-based SO₂-resistant NH₃-SCR catalysts, specifically focusing on the synthesis and interaction of nanomaterials.

Keywords: SBA-15; rare earth; NH₃-SCR; CeO₂; nanosphere; SO₂ resistance



Citation: Han, X.; Bian, M.; Liu, K.; Yang, X.; Zheng, D.; Yang, X.; Zhang, Y. Influence of Particle Size of CeO₂ Nanospheres Encapsulated in SBA-15 Mesopores on SO₂ Tolerance during NH₃-SCR Reaction. *Catalysts* **2024**, *14*, 151. <https://doi.org/10.3390/catal14020151>

Academic Editors: Stefano Cimino and Leonarda Liotta

Received: 31 December 2023

Revised: 2 February 2024

Accepted: 13 February 2024

Published: 18 February 2024



Copyright: © 2024 by the authors. Licensee MDPI, Basel, Switzerland. This article is an open access article distributed under the terms and conditions of the Creative Commons Attribution (CC BY) license (<https://creativecommons.org/licenses/by/4.0/>).

1. Introduction

NO_x, including NO and NO₂, is a common air pollutant from industrial boilers [1–4]. Selective catalytic reduction with NH₃ (NH₃-SCR) has been used for a long time as an effective method of purification [5,6]. Due to its outstanding oxygen storage capacity (OSC), ceria (CeO₂) and modified Ce-based catalysts have attracted much attention from researchers to rare earth heterogeneous catalysts for NH₃-SCR [7,8]. However, pure CeO₂ nanocatalysts have a low catalytic activity, partly due to their low surface acidity and agglomeration effects caused by particle aggregation [9,10]. One way to solve this problem is to prepare supported Ce-based catalysts, and the specific surface area should be considered when choosing a suitable support. For example, SBA-15, a mesoporous silica molecular sieve with a high surface area of about 400 m²/g, constitutes a promising support material for catalytic applications [11]. Shen et al. used SBA-15 as a support to synthesize CeO₂/SBA-15 catalysts and focused on the effect of a P123 template on the attachment of CeO₂ to the surface of SBA-15 [12]. Their results showed that SBA-15 could be a great support, while P123 was a template which increased the dispersion of CeO₂.

Currently, the deactivation of catalysts caused by SO₂ poisoning has become an extremely serious problem for Ce-based NH₃-SCR catalysts. The adsorption of SO₂ on the surface of the catalyst and the subsequent oxidation generating SO₃ and Ce₂(SO₄)₃ are

steps taking place above a temperature of 300 °C, alongside the formation of ammonium sulfate (AS) and ammonium bisulfate (ABS). After the above, these sulfate bulks cover the active centers, leading to a sharp drop in catalytic activity. Furthermore, the active centers of supported CeO₂-based catalysts may transfer to the contact surface or be limited by the structure of the supports [13]. This phenomenon results in different numbers and densities of active centers due to the different sizes of CeO₂-based particles [14]. Ma et al. synthesized a novel hollow structure where TiO₂ was the shell and C@CeO₂ was the core [15]. They compared the SO₂ resistance of shells with different sizes: 5 μm and 400 nm. Their test data showed that larger shells had better SO₂ resistance. They only explained the effect of AS and ABS on the catalyst and how large shells counteracted this effect, but they did not explore the effect of the particle size of the CeO₂. Hu et al. used the wet impregnation method to prepare CeO₂/MoO₃(nanorods) catalysts [16]. The size of the CeO₂ was controlled by the amount of Ce(NO₃)₃ added. They found that smaller CeO₂ particles had more non-bulk electronic states, which increased the rejection of SO₂ adsorption. However, the impregnation method they used led to an uneven distribution and an inconsistent morphology of the introduced CeO₂ particles, resulting in not only considering particle size as a single variable between different samples but also affecting subsequent studies.

Nanospheres have garnered significant attention in the areas of material synthesis and application due to their regular crystal planes and uniform morphology. Li et al. synthesized Mn-doped CeO₂ nanospheres for NH₃-SCR, demonstrating that these nanospheres had a better performance than those prepared using the co-precipitation method [17]. However, in current studies, little focus has been given to the sulfur resistance of nanospheres, which is an important parameter for their applications. Moreover, the impact of particle size on the properties of these nanospheres has not been well understood.

In this study, CeO₂ nanospheres with varying diameters were synthesized and supported by an SBA-15 molecular sieve. The focus was on the performance of NH₃-SCR and SO₂ resistance. After determining the optimal loading percentage for maximum catalytic activity, four different sizes of CeO₂ nanospheres (5 nm, 6 nm, 7 nm, and 9 nm) were prepared and loaded onto SBA-15 at the determined optimal loading percentage. The particle size of the CeO₂ nanoparticles was determined using a laser particle size analyzer and TEM. XRD, FT-IR, H₂-TPR, NH₃-TPD, and XPS were used to investigate the structure, physical and chemical properties, and electronic state of the CeO₂/SBA-15 catalysts. The catalytic performance was evaluated on a fixed-bed reactor with an online infrared gas analyzer, and the impact of SO₂ was assessed by decreased catalytic efficiency. Additionally, possible reaction mechanisms for these nanosphere catalysts were proposed to better understand the NH₃-SCR reaction via in situ DRIFTS.

2. Results and Discussion

2.1. Pore Analysis of SBA-15

SBA-15, which was purchased from XFnano in Nanjing, PRC, was the support of the CeO₂ nanospheres. The investigation of its pore structure was helpful in selecting the appropriate particle size of the nanospheres in the preparation process. A N₂ isotherm adsorption and desorption test was performed on this molecule sieve. The textural data of these samples are listed in Table 1. It can be found that the BET specific surface area of SBA-15 is as high as 496 m²/g, while the mean pore diameter is 10.07 nm. In addition, the BJH pore distribution curves are shown in Supplementary Figure S1. It can be seen that all of those pores are located in the mesopore range of a 6~12 nm diameter. To give the active components (nanospheres) a chance to arrive inside the support, CeO₂ nanospheres with diameters of 5~9 nm were synthesized.

Table 1. BET specific surface area, pore volume, and mean pore diameter of SBA-15.

Sample	BET Surface Area (m ² /g)	Pore Volume (cm ³ /g)	Average Pore Diameter (nm)
SBA-15	496	1.20	10.07

2.2. Particle Size Control of Nanospheres

Polyvinylpyrrolidone (PVP), a surfactant, has been found to play a crucial role in the oriented aggregation process of CeO₂ nanoparticles [18,19]. Zhang et al. observed that the size of CeO₂ nanocrystals initially decreased and then increased with an increase in the amount of PVP added [20]. When the concentration of PVP was low, it attached itself to the surface of CeO₂ seed crystals, inhibiting the growth of active crystal planes. However, as more PVP was added, the inhibition became more pronounced, leading to a decrease in particle size. The particle size of CeO₂ nanospheres could be precisely controlled by adjusting the amount of PVP added in 40 mL of ethanol. Microscopic observation of these nanospheres was performed using TEM, and the particle size was measured using the ImagePro6.0 software. The results are presented in Figure 1, where four different PVP addition amounts were used to control the particle size of nanospheres within the range of 5–9 nm. It is also evident that the more PVP is added, the smaller the particle size of the nanospheres that can be synthesized. Furthermore, the laser particle size analyzer data for the different particle sizes of CeO₂ nanospheres are presented in Figure S2 and Table S1.

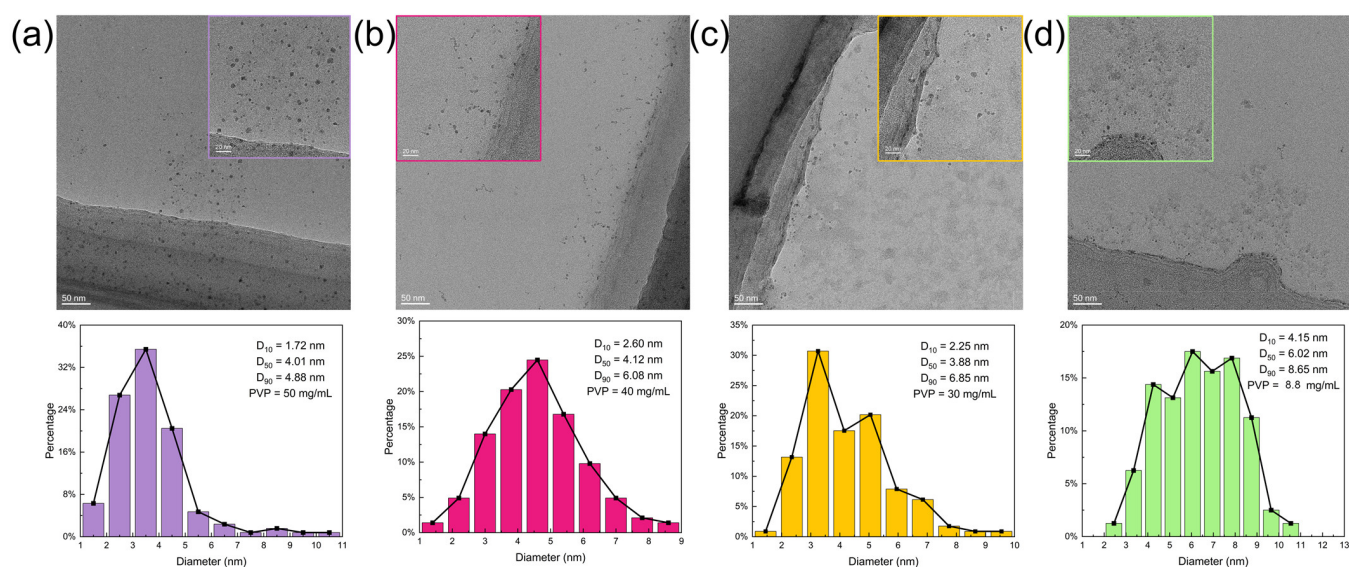


Figure 1. TEM images and particle size statistics from TEM images of different PVP amounts in ethanol. (a) 50 mg/mL, D₉₀ = 5 nm; (b) 40 mg/mL, D₉₀ = 6 nm; (c) 30 mg/mL, D₉₀ = 7 nm; and (d) 8.8 mg/mL, D₉₀ = 9 nm.

2.3. NH₃-SCR Performance and SO₂ Resistance of the Catalyst

According to the selected four different particle sizes, we selected the particle size in the middle for the preparation of catalysts with different loading percentages. Nanospheres 7 nm in diameter were used as an ingredient to prepare five catalysts with loading percentages of 5%, 15%, 25%, 35%, and 45%. After the catalytic activity test, the data are plotted in Figure S3. It can be clearly seen from Figure S3a that the 7n-Ce/SBA had the best NH₃-SCR performance, converting 92% of NO_x at a temperature of 300 °C, which was the highest NO_x conversion of these catalysts. Compared to 7n-Ce/SBA, 7n-Ce/SBA(45%) showed the same catalytic performance before 300 °C, while, with the temperature increasing, its NO_x conversion dropped quickly. The NO_x conversion of other catalysts including pure CeO₂ did not exceed 80% at 300 °C. Furthermore, except for 7n-Ce/SBA(25%) and 7n-Ce/SBA(5%), which had the best activity temperature of 350 °C, the temperature of

the best SCR performance for the rest of the catalysts was 300 °C. In addition to this, the performance of pure 7n-Ce/SBA(5%) was worse than that of the 7 nm CeO₂ nanospheres, because of the fewer activity sites. Moreover, Figure S3b shows that N₂ selectivity was almost the same for these samples, except for 7n-Ce/SBA(15%). Their N₂ selectivity decreased from 98% to 95% with the increase in temperature. However, 7n-Ce/SBA(15%) showed a trend of dropping first and then rising. The NO_x purification performance of the nanospheres with a bigger size was also investigated. Figure S3c depicts CeO₂ nanospheres with a D₉₀ of 32 nm, which were obtained by adjusting the amount of PVP added. The resulting catalyst was designated as 30n-Ce/SBA. The NO_x conversion curve of this catalyst is plotted in Figure S3d. As can be observed from the figure, 30n-Ce/SBA exhibits an enhanced stability compared to 5n-Ce/SBA, and its activity remains relatively stable even after the introduction of SO₂. However, the denitrification performance of the catalyst deteriorates significantly in the absence of SO₂. Therefore, it can be concluded that larger particle sizes are more favorable. Consequently, the size range of the nanospheres studied in this work is justified.

After determining the optimal loading percentage of these catalysts, the CeO₂ nanospheres with 5, 6, 7, and 9 nm diameters were loaded on SBA-15. These samples were tested for SCR performance, and the results are shown in Figure 2a. As can be seen from the data in Figure 2a, 9n-Ce/SBA, which converted 90% of NO_x at 300 °C, had the best catalytic performance. 7n-Ce/SBA had a better activity than 9n-Ce/SBA below 300 °C, and it purified 80% of NO_x at 250 °C. Moreover, the catalytic activity of 5n-Ce/SBA was significantly higher than that of 6n-Ce/SBA, the worst one out of these catalysts. As described in Figure 2b, the N₂ selectivities of these catalysts were very close to one another and were all above 90%, except for the pure CeO₂. The N₂ selectivity of 9n-Ce/SBA was the lowest below 250 °C, while it became the highest when the temperature of the reactor reached more than 300 °C, as indicated by the green line in Figure 2b.

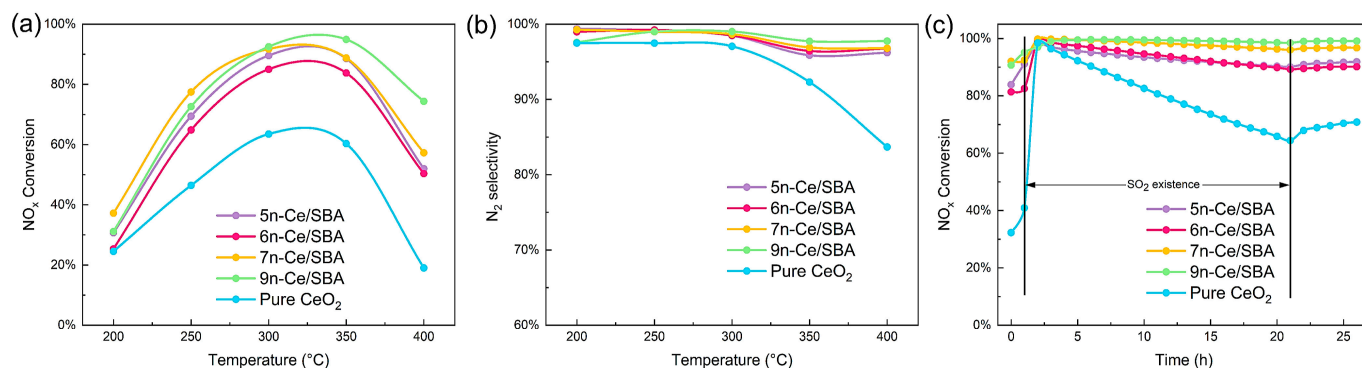


Figure 2. NO_x conversion (a) and N₂ selectivity (b) curves of CeO₂/SBA-15 catalysts with different particle sizes and pure CeO₂. (c) NO_x conversion curves of catalysts with different particle sizes and pure CeO₂ in 100 ppm SO₂ existing for 20 h.

Figure 2c shows the NO_x conversion data of CeO₂/SBA-15 catalysts with different particle sizes when 100 ppm SO₂ was added to the gas. All the catalysts stabilized at 300 °C for 1 h without SO₂. When the SO₂ gas was introduced into the reactor, the activity of the CeO₂ catalysts improved quickly in 1 h because of the beneficial effects of a small amount of sulfate, which had no effect on SCR but increased the surface acidity of CeO₂ [21,22]. The existence of Ce₂(SO₄)₃ enhanced the adsorption ability of CeO₂ to NH₃, promoting NH₃-SCR performance. However, as the amount of sulfate increased, the activity of all the catalysts showed a decreasing trend 1.5 h after the introduction of SO₂. When SO₂ was continuously introduced, NH₃, O₂, and SO₂ formed sulfate that attached to the surface of the catalysts and covered the active sites. 9n-Ce/SBA, which converted 99.5% of NO_x with the presence of SO₂, had the best SO₂ tolerance. Its activity hardly decayed during the entirety of the 26 h test. And the NO_x conversion of 7n-Ce/SBA decreased from 100%

to 95% during the 20 h of SO₂ presence, which was significantly higher than those of 6n-Ce/SBA and 5n-Ce/SBA. One unanticipated finding was that the activity of 6n-Ce/SBA was higher than that of 5n-Ce/SBA in the first 15 h, while it dropped rapidly, meaning that 5n-Ce/SBA had the better performance of the two when the test ended.

After turning off the SO₂ switch, the NO_x conversion of all the catalysts was recovered but was still lower than the catalytic efficiency measured when SO₂ was first introduced. This finding was understandable because Ce₂(SO₄)₃ was no longer formed, while AS and ABS could slowly decompose at 300 °C [23,24]. Moreover, it is evident from Figure 2a,c that the order of catalytic activity in the presence of SO₂ was consistent with the order of catalytic activity without SO₂. 9n-Ce/SBA always maintained a leading position. These results suggested that both Ce₂(SO₄)₃ and ammonia sulfide were the causes of catalyst deactivation.

2.4. Material Structure and Morphology

2.4.1. Phase Analysis (XRD and FT-IR)

X-ray diffraction is one of the most commonly used phase analysis methods. It can determine the crystal structure of CeO₂. The corresponding results are given in Figure 3a. According to JCPDS #34-0394, a series of diffraction peaks at $2\theta = 28.55^\circ, 33.08^\circ, 47.48^\circ, 56.33^\circ, 59.09^\circ, 69.40^\circ, 76.70^\circ,$ and 79.07° were ascribed to different crystal planes of cubic fluorite-type CeO₂. The characteristic intensity diffraction peaks of (1 1 1) and (2 2 0) gradually decreased with the increase in particle size. The reason may be that the catalysts with smaller particle sizes exposed a higher density of crystal planes, which led to an increase in the diffraction intensity.

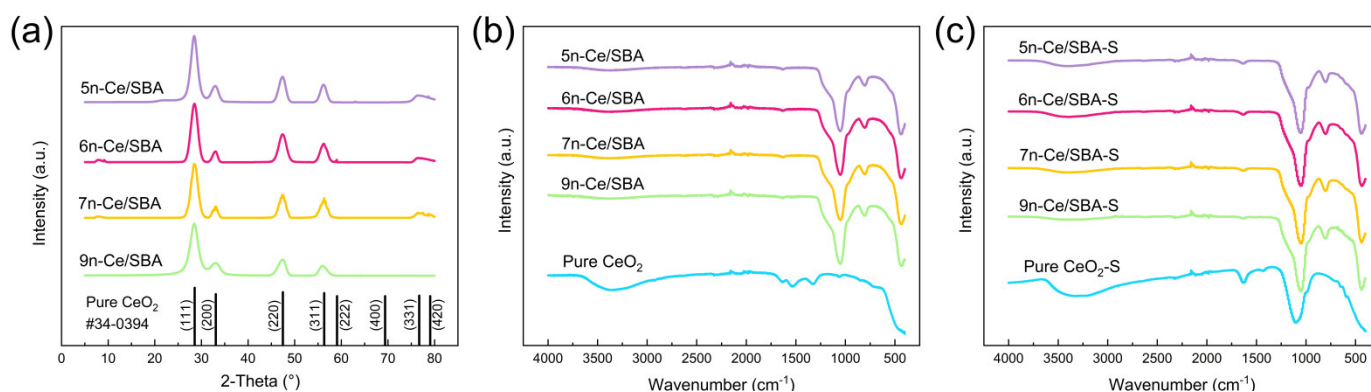


Figure 3. (a) XRD patterns of CeO₂/SBA-15 catalysts with different particle sizes and a standard PDF card of CeO₂ (#34–0394). Infrared absorptivity of CeO₂/SBA-15 catalysts (b) before and (c) after the 20 h SO₂ resistance test with different particle sizes and pure CeO₂.

Moreover, the Ce/SBA catalysts before SO₂ poisoning were characterized by FT-IR. The absorption spectrum of these catalysts is plotted in Figure 3b. The absorption peak from 1100 to 1000 cm^{−1} is the stretching vibration of the Si–O bond [25]. Since SBA-15 makes up the majority of the catalyst, the intensity of these peaks does not change with the increase in particle size. And, the SO₂-poisoned catalysts were also tested by FT-IR, the results of which are shown in Figure 3c. The spectrum of pure CeO₂-S exhibits a prominent absorption peak at the position of 1100 cm^{−1}, indicating the presence of a considerable amount of sulfate on the catalyst [26]. Conversely, the IR peaks of the Ce/SBA series of catalysts remain unchanged, suggesting that the sulfate produced on these catalysts is too minute to be detected by IR spectroscopy, which is consistent with their SO₂ resistance capabilities.

2.4.2. Morphology of Catalysts (TEM)

TEM is a common method of observing the morphology of materials. TEM photos of the four catalysts and of the EDS distribution of the S element are shown in Figure 4. The figure reveals that the nanospheres were aggregated on all four catalysts, which corresponded

to 35% of their loading capacity. Additionally, a comparison between Figure 4a,b reveals that, after being contaminated with sulfur, the catalysts maintained their morphology as nanospheres and nanosheets. Due to the aggregation of nanospheres, it is challenging to distinguish between the dark region in the images and whether it is a nanosphere or sulfate. Consequently, we photographed the EDS spectrum of the catalyst, which is presented in Figure S4. Furthermore, the distribution of the S elements is plotted in Figure 4c. By examining both Figure S4 and Figure 4c, the distribution of sulfur elements can be observed on all four catalysts. When analyzed in conjunction with the high-angle annular dark field (HAADF) photo, it becomes evident that there are more S elements present in the white bright spots (areas where the CeO_2 nanospheres congregate) in the figure. This suggests that S elements preferentially react with CeO_2 to form cerium sulfate.

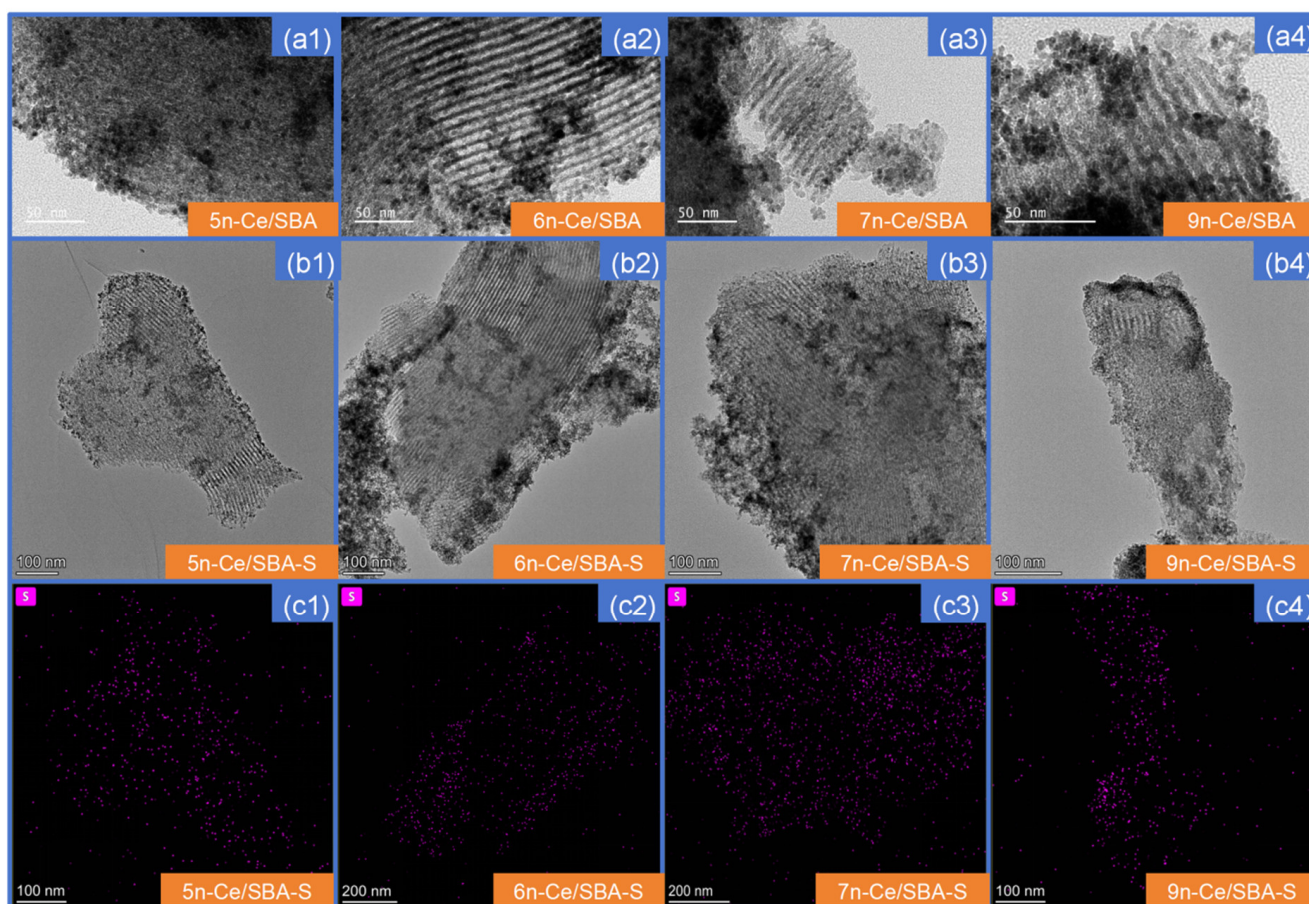


Figure 4. TEM images of (a1–a4) Ce/SBA and (b1–b4) Ce/SBA-S-series catalysts. Panes (c1–c4) are the EDS mapping of sulfur on Ce/SBA-S-series catalysts.

2.5. Chemisorption Test

2.5.1. Acid Site Distribution and Intensity (NH_3 -TPD)

NH_3 -TPD is a common means of characterizing catalyst surface acidity. It can detect the strength and number of acid sites on the catalyst's surface. In Figure 5a, all the desorption curves of CeO_2 /SBA-15 catalyst, pure CeO_2 , and SBA-15 can be observed in a temperature range of 50 to 500 °C. The detector also recorded the amount of NH_3 leaving the catalyst surface during the desorption process, and these data are presented in Table S2. The first peak located around 100 °C is related to the physically adsorbed NH_3 [27]. And, the other two peaks represent the NH_4^+ adsorbed by Bronsted acid (around 150 °C) and the coordinated NH_3 bound to the Lewis acid sites (around 280 °C) [28]. According to the total NH_3 consumption, it can be found that the minimum NH_3 consumption of the supported Ce/SBA catalyst is 0.242 mmol/g, which is close to that of pure CeO_2

(0.241 mmol/g) and SBA-15 (0.240 mmol/g). The acidity of the 9 nm CeO₂ nanospheres, SBA-15, and 5n-Ce/SBA can be considered equivalent. However, the 9n-Ce/SBA catalyst, which comprises 35% 9 nm CeO₂ nanospheres and 65% SBA-15 molecular sieve (mass ratio), exhibits a higher acidity (0.315 mmol/g) than the sum of the 9 nm CeO₂ nanospheres and SBA-15 with the same weight. This result combined with the difference in the peak 2 area in Table S2 suggests an interaction between the 9 nm CeO₂ nanospheres and SBA-15. This interaction increases the number of Bronsted sites on the catalyst and enhances its adsorption capacity for NH₃. More importantly, the peak area, indicating the number of acidic sites, is significantly correlated with NH₃-SCR performance. The peak areas at temperatures of about 150 °C and 300 °C for the four curves increase sequentially from top to bottom, and they are all larger than that of pure CeO₂, which is consistent with the ranking of catalytic activity with the presence of SO₂. This can explain why 9n-Ce/SBA can have the highest NH₃-SCR performance and pure CeO₂ the lowest one. And it can also be inferred that, since SO₂ is an acidic gas, it tends to be adsorbed onto less acidic substances. Therefore, the more acidic the catalyst, the less likely it is to adsorb SO₂. The data from the NH₃-TPD analysis suggest that the 9n-Ce/SBA catalyst may exhibit excellent SO₂ resistance due to its low adsorption rate of SO₂, resulting in reduced sulfate production after SO₂ adsorption at the active site. This reduction in the sulfate formation rate helps to minimize the amount of poisoning at the active site, contributing to the excellent sulfur resistance of the catalysts.

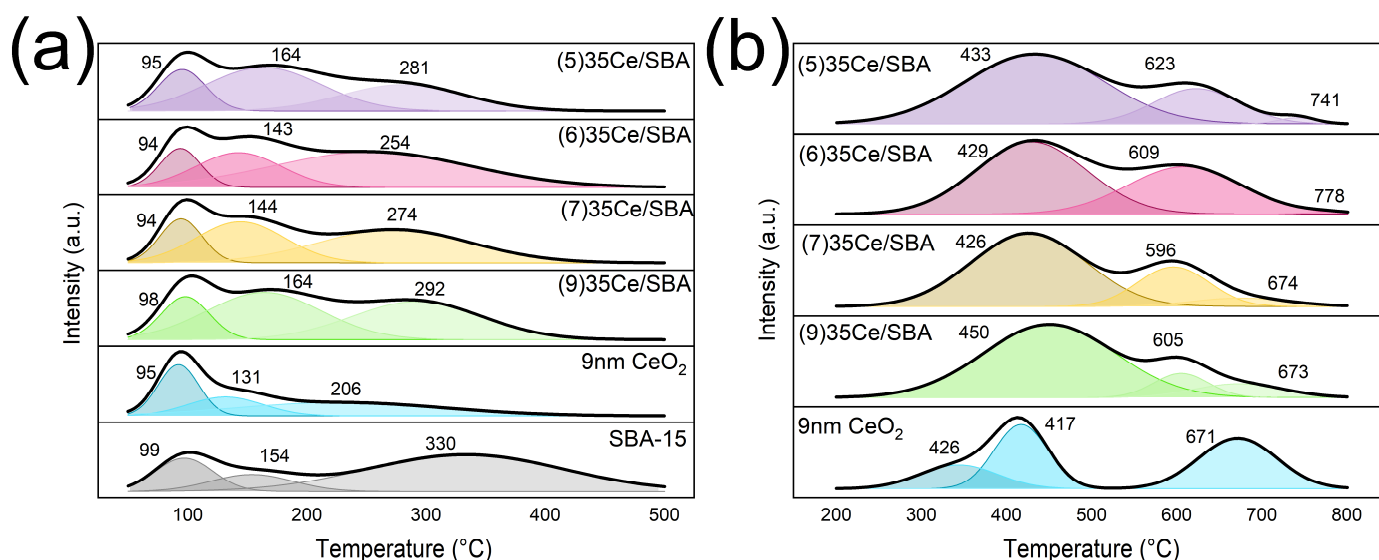


Figure 5. (a) NH₃-TPD and (b) H₂-TPR curves of CeO₂/SBA-15 catalysts with different particle sizes, pure CeO₂, and SBA-15.

2.5.2. Redox Site Distribution and Intensity (H₂-TPR)

The oxidation process is an important part of the SCR mechanism. In the process of SCR, there must be oxidation and reduction of substances. The oxidation performance of a catalyst is closely related to its catalytic activity. H₂-TPR can be used to characterize the oxidative capacity of CeO₂/SBA-15 catalysts, and the results are shown in Figure 5b. The consumption of H₂ is counted in Table S3. SBA-15 cannot be reduced by H₂ within 800 °C, indicating that the reduction peak in Figure 5b is solely attributed to CeO₂. For pure CeO₂, its H₂-TPR curve exhibits three peaks, namely, surface-adsorbed oxygen, surface Ce⁴⁺, and volume-phase Ce⁴⁺ from a low temperature to a high temperature [29]. These peaks are consistent with those of the pure 9 nm CeO₂ in Figure 5b. Furthermore, the graph provides some information on the fact that the addition of SBA-15 makes the three reduction peaks move to a high temperature, indicating an increase in the strength of the oxidative sites because of the mutual effect between SBA-15 and the nanospheres. And, due to the high

dispersion of the CeO₂ nanospheres on the surface and in the poles of the SBA-15, the width of the first peak increases. Moreover, the reduction peak of adsorbed oxygen for the 9n-Ce/SBA catalyst is at 450 °C, which is significantly higher than that of the other catalysts. This suggests that the oxidation capacity of this catalyst is weaker compared to the other catalysts. This trend indicates that a smaller particle size of the nanospheres has a stronger oxidation activity, which can both improve the SCR performance and the probability of side reactions such as SO₂ oxidation, causing catalysts' poisoning. The data from the NH₃-TPD analysis and the observation of the reduction peak of adsorbed oxygen for the 9n-Ce/SBA catalyst in Figure 4 lead us to the conclusion that this catalyst exhibits exceptional SO₂ resistance. The reason behind this is that SO₂ is not easily adsorbed onto the surface of the catalyst, as evidenced by the stronger NH₃ desorption intensity. Additionally, after being adsorbed, SO₂ is not easily oxidized by surface-active oxygen, resulting in the lowest generation of sulfates on this catalyst. This phenomenon leads to a minimal amount of poisoning at the active site, contributing to the superior SO₂ resistance of the 9n-Ce/SBA catalyst.

2.6. Valence Testing of Surface Atoms (XPS)

X-ray photoelectron spectroscopy (XPS) is a surface analysis technique that can characterize the atomic species on the surface of a material and the valence state of an ion through the electronic states. In this work, XPS was used to study the chemical state and surface properties of CeO₂/SBA-15 catalysts. The XPS spectra of Ce 3d of the Ce/SBA catalysts before SO₂ poisoning is presented in Figure 6a, and it can be seen that there are eight peaks of the Ce 3d orbital. The letters U and V stand for the orbitals after splitting, named 3d_{3/2} and 3d_{5/2}, located at 902.5 eV and 882.5 eV, respectively. The characteristic peaks labeled as V' (885.6 eV) and U' (904.2 eV) represent the initial electronic state of the 3d¹⁰4f¹ of the Ce³⁺ ion, while the other six peaks marked as U, U'', U''', V, V'', and V''' are the characteristic peaks of Ce⁴⁺ with the electronic state of 3d¹⁰4f⁰ [9,29]. The results of the XPS demonstrate that both Ce⁴⁺ and Ce³⁺ exist in these CeO₂/SBA-15 catalysts. The presence of Ce³⁺ on the catalyst can disrupt charge balance and cause oxygen vacancies, which facilitates the adsorption of oxygen in the gas on the surface, thereby improving the efficiency of the oxidation process in the NH₃-SCR reaction [30]. Moreover, Table 2 gives the content of Ce³⁺ and the Ce³⁺/Ce⁴⁺ ratio on the surface of these catalysts. The relative Ce³⁺ content of the xn-Ce/SBA (x = 5, 6, 7, and 9) catalysts is 22.80%, 26.00%, 21.43%, and 27.70%, respectively. It can be found that 9n-Ce/SBA has the most Ce³⁺ content, but this value is not much higher than that of the other samples. Therefore, the content of Ce³⁺ on the surface is not a decisive factor for the resistance to SO₂. This can also be seen from the XPS spectra of the sulfurized catalyst, as shown in Figure 6b. After SO₂ treatment, the proportion of Ce³⁺ on the catalyst has no significant change compared to that before poisoning and is maintained at about 25%. For example, for the 9n-Ce/SBA with the best NH₃-SCR performance, the Ce³⁺ before poisoning was 27.70%, but, after poisoning, the Ce³⁺ was slightly reduced to 23.57%, indicating that SO₂ poisoning ultimately did not affect the valence state of Ce.

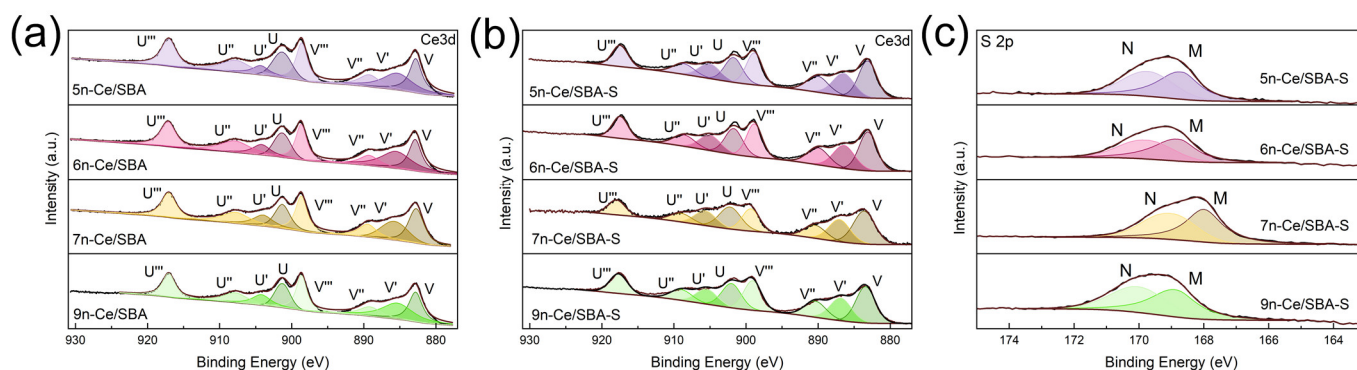


Figure 6. XPS spectra of (a) Ce 3d of Ce/SBA catalysts, (b) Ce 3d, and (c) S 2p of Ce/SBA-S catalysts.

Table 2. Surface element contents of the catalysts, derived from XPS spectra.

Catalyst	Ce ³⁺ /(Ce ³⁺ + Ce ⁴⁺)	Ce Atoms on Surface (Atomic Percentage)	S Atoms on Surface (Atomic Percentage)
5n-Ce/SBA	22.80%	5.79%	
6n-Ce/SBA	26.00%	2.52%	—
7n-Ce/SBA	21.43%	2.68%	
9n-Ce/SBA	27.70%	2.41%	
5n-Ce/SBA-S	24.01%	4.46%	1.28%
6n-Ce/SBA-S	23.98%	4.64%	1.79%
7n-Ce/SBA-S	25.72%	1.58%	5.63%
9n-Ce/SBA-S	23.57%	5.36%	3.05%

In Figure 6b and Table S4, the location of the main Ce 3d peak (peak V) for each catalyst varies, and it shifts from 883.19 eV to 883.50 eV as the particle size increases. In contrast, the binding energy of peak V of the 30n-Ce/SBA catalyst is 882.99 eV, which is lower than the other catalysts. This observation indicates that CeO₂ nanoparticles of different sizes interact with Si and S atoms on the catalyst surface. Table 2 shows the proportion of S atoms on the catalyst surface, and it can be observed that 9n-Ce/SBA has a mutual effect with Si. Because the S element in 9n-Ce/SBA accounts for 3.05% of it, the movement of its binding energy is higher than that of 7n-Ce/SBA, whose S element proportion is 5.63%. It is well known that SiO₂ fundamentally does not react with SO₂ and has strong structural and chemical stability. Therefore, 9n-Ce/SBA can reduce the probability of a reaction with SO₂ by virtue of this close effect and, thus, show excellent SO₂ resistance.

2.7. Sulfation Rate Test of Active Components

In the sections above, several characterization methods such as NH₃-TPD, H₂-TPR, and XPS were employed to demonstrate that 9n-Ce/SBA has the highest acidity and exhibits weak adsorption and reduction by SO₂. To further substantiate this claim, SO₂ and O₂ were introduced into the reactor to examine the rate at which the active component was cured, as shown in Figure 7. From the figure, it can be seen that 5n-Ce/SBA, 6n-Ce/SBA, and 9n-Ce/SBA quickly adsorb all the SO₂ gas. But 9n-Ce/SBA maintains a 100% conversion of SO₂ for the longest time out of all the catalysts, i.e., about 30 min. The other three samples keep a 100% conversion for 20 min, while 7n-Ce/SBA takes more time to adsorb all of the SO₂, which shows a weaker oxidation ability than 5n-Ce/SBA and 6n-Ce/SBA. Table S5 presents the BET specific surface area of the catalysts, and it can be observed that all four catalysts have similar specific surface areas of about 350 m²/g. Therefore, the endurance time under the SO₂ atmosphere is not significantly affected by the specific surface area of a catalyst. From Figure 7, it can be inferred that the active component of 9n-Ce/SBA has the lowest sulfurization rate, and it accumulates less sulfate after being exposed to SO₂ for the same duration (e.g., during the reaction of NH₃-SCR containing SO₂ for 20 h). This proves that 9n-Ce/SBA has the strongest SO₂ resistance among the four catalysts. In conjunction with the TEM image presented in Figure 4, it is evident that certain nanospheres on the catalyst exhibit agglomeration. A correlation between the specific surface area analysis and nanosphere agglomeration reveals that the smaller specific surface areas of the catalyst result in a more pronounced agglomeration of nanospheres. Moreover, the nanospheres present on the catalysts' surface, ready to combine with the SO₂, forming cerium sulfate. Consequently, the 5n-Ce/SBA and 6n-Ce/SBA catalysts, characterized by smaller specific surface areas, exhibit inferior SO₂ tolerance.

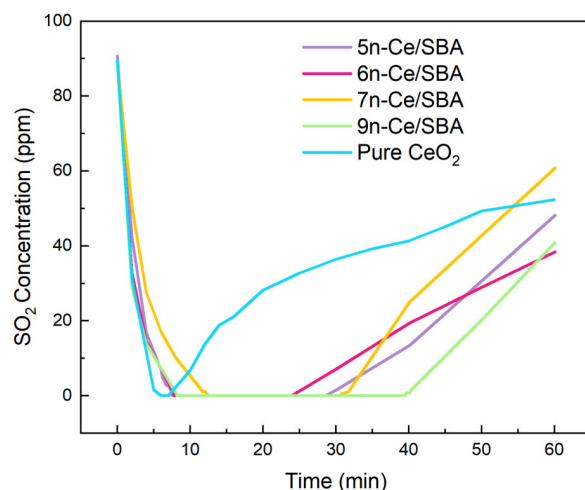


Figure 7. SO₂ concentration curves in the outlet of the reactor of catalysts with different particle sizes in 100 ppm SO₂ and 5% O₂ for 1 h.

2.8. Reaction Kinetics

Catalytic reaction kinetics is a field of study that explores the relationship between the rate of a catalytic reaction and various process variables. The primary objective of this research is to gain a deeper understanding of the underlying mechanisms behind catalytic reactions, which can then be used to inform catalyst design. To achieve this goal, rate equations have been developed for the catalytic reaction of NO, NH₃, and O₂ with respect to the catalysts. These equations are aimed at identifying any specific mechanisms that may be involved in the reaction process. Table 3 presents data on the order of reaction and rate equations for several catalysts used in NH₃-SCR reactions. Additionally, Figure S7 illustrates the relationship between reaction rate r and reactant concentration. Firstly, it can be observed that the catalysts exhibit a different reactivity towards NO. The reaction orders for 5n-Ce/SBA and 6n-Ce/SBA are slightly higher than 0.6, while the order of 7n-Ce/SBA is the highest, at 0.818. The reaction order of NO for 9n-Ce/SBA is 0.717. These values are all less than 1, suggesting that some NO does not adsorb into the catalysts, indicating the coexistence of L-H and E-R mechanisms in the catalysts. Secondly, the reaction order of the catalysts towards NH₃ is very small, almost close to 0, indicating that, when the concentration of NH₃ exceeds 400 ppm, the adsorption of NH₃ by the catalysts is near saturation. Under optimal conditions, where the NH₃/NO ratio is 1:1, there is no excess NH₃, and it does not escape from the flue gas. Finally, the NO_x conversion of the catalysts in the range of a 1~5% oxygen concentration is not significant, suggesting that, at an oxygen concentration above 1%, the catalysts form a large number of adsorbed oxygen and lattice oxygen, enhancing its surface oxidation capacity.

Table 3. Reaction orders and rate equations for NH₃-SCR with Ce/SBA catalysts.

Catalyst	Reaction Order of			Rate Equation
	NO	NH ₃	O ₂	
5n-Ce/SBA	0.604	0.00041	0.138	$r = k[\text{NO}]^{0.604}[\text{NH}_3]^{0.00041}[\text{O}_2]^{0.138}$
6n-Ce/SBA	0.631	0.00050	0.112	$r = k[\text{NO}]^{0.631}[\text{NH}_3]^{0.00050}[\text{O}_2]^{0.112}$
7n-Ce/SBA	0.818	0.00045	0.099	$r = k[\text{NO}]^{0.818}[\text{NH}_3]^{0.00045}[\text{O}_2]^{0.099}$
9n-Ce/SBA	0.717	0.00032	0.115	$r = k[\text{NO}]^{0.717}[\text{NH}_3]^{0.00032}[\text{O}_2]^{0.115}$

2.9. Thermal Decomposition of Sulfate (TGA)

The thermogravimetric analysis of Ce/SBA-S-series catalysts was conducted to determine the types and thermal decomposition temperatures of the sulfur-containing substance present on the catalysts. The TG and DSC curves are presented in Figure 8. After being

reacted with in the presence of 500 ppm NO, 500 ppm NH₃, and 100 ppm SO₂ with 5 vol% O₂ (balanced with N₂) for 20 h at 300 °C, the TG curves of these catalysts exhibited two significant weight loss events at temperatures ranging from 306 to 418 °C and from 1015 to 1042 °C, accompanied by two exothermic peaks in the DSC curves. These first weight loss events corresponded to the decomposition of ABS and AS, while the second event corresponded to the pyrolysis of cerium sulfate, respectively. By comparing the mass ratio of ABS and AS, it can be observed that the ammonium (bi)sulfate on the 9n-Ce/SBA-S catalyst was the least present, at only 2.44%, while this substance's proportion on the 6n-Ce/SBA-S catalyst with poor SO₂ resistance was 4.27%. Similarly, by analyzing the mass ratio of cerium sulfate, it can be seen that the cerium sulfate deposited on the 9n-Ce/SBA-S catalyst was only 4.19%, while the cerium sulfate on the 6n-Ce/SBA-S catalyst was as high as 5.61%. These results indicate that the 9n-Ce/SBA-S catalyst accumulated the least amount of sulfate substances during the reaction, which is consistent with the results of the NH₃-TPD, H₂-TPR, and XPS tests and the sulfurization rate of the active components.

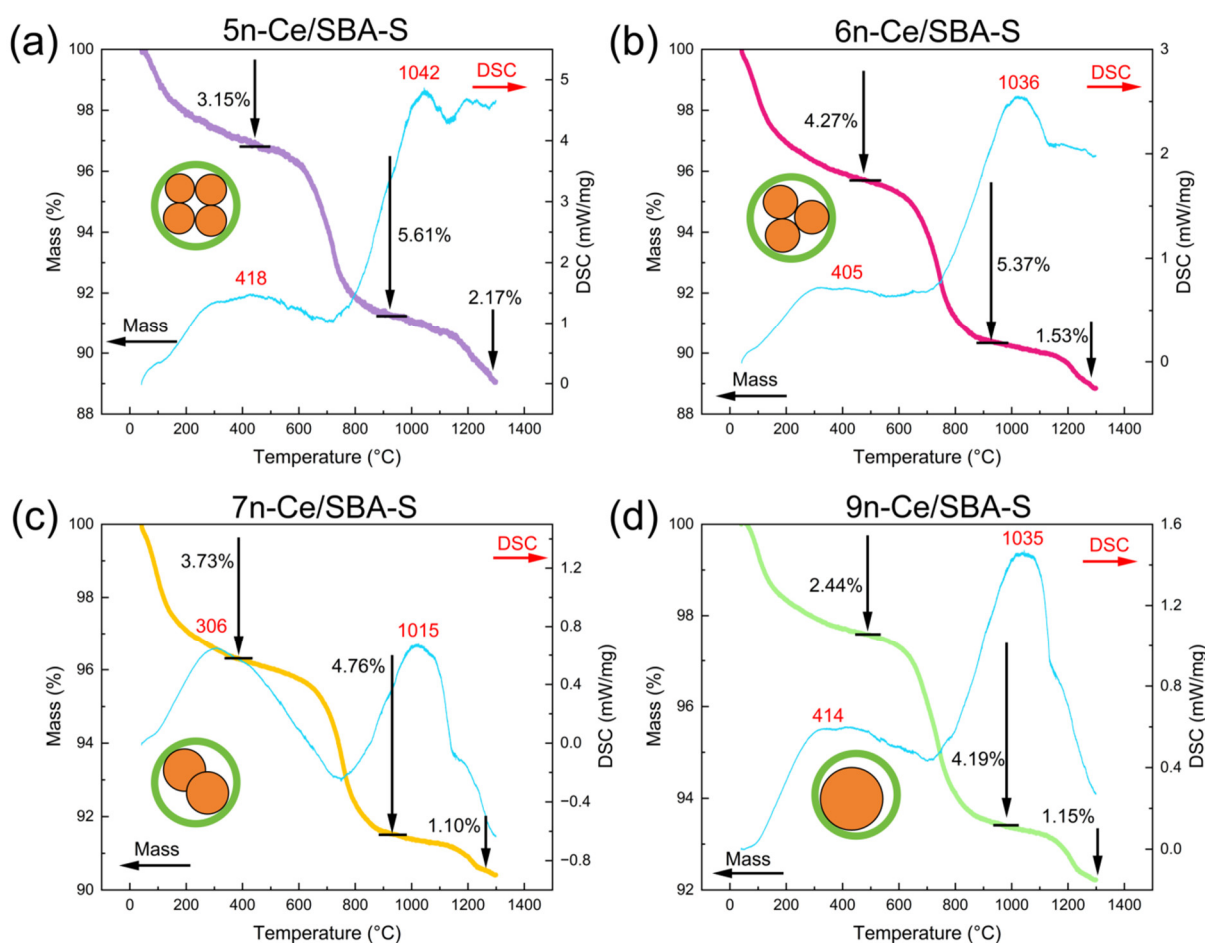


Figure 8. Ex situ TG-DTA curves of Ce/SBA catalysts after being treated with NH₃, NO, O₂, and SO₂. (a) 5n-Ce/SBA-S, (b) 6n-Ce/SBA-S, (c) 7n-Ce/SBA-S and (d) 9n-Ce/SBA-S.

2.10. Reaction Mechanism

In situ DRIFT spectroscopy was used to investigate the active intermediates and mechanisms in the catalysts before and after SO₂ poisoning. The adsorption of 9n-Ce/SBA and 9n-Ce/SBA-S on NH₃ and NO as well as surface reactions were analyzed using this technique. The catalysts were tested for NH₃ adsorption and NO adsorption at different temperatures to examine the species and strength of the acid sites on the catalysts' surface, particularly the acidity enhanced by SO₂, and the types of intermediates (nitrates) formed on the catalysts by NO and NO₂. The IR spectra obtained from these tests are presented in

Figures S8 and S9. Additionally, the reactions of NH_3 , NO , and O_2 were also monitored by in situ DRIFTS, and the results are shown in Figure S10. The test conditions and the results' analysis can be found in the Supplementary Materials.

Based on our previous research and the literature, we observed a peak at 3300 cm^{-1} that can be attributed to the stretching vibration of the N-H bonds of coordinated NH_3 species. Additionally, the peaks from 1419 to 1439 cm^{-1} suggest the presence of Bronsted acid sites and NH_4^+ species on the catalysts' surface [31,32]. Moreover, the lattice oxygen in the catalysts was active, leading to the appearance of IR peaks at 1338 and 1327 cm^{-1} , which are attributed to oxidized NH_3 species [33]. The orange lines in the figures represent the IR absorption peaks of the nitrate species. The peak located at 1535 (1539) cm^{-1} is assigned to monodentate nitrate, while the band at 1578 cm^{-1} represents bidentate nitrate. Furthermore, M- NO_2 nitro compounds with their IR peak at 1315 (1304) cm^{-1} and NO_2^- with its asymmetry vibration IR peak at 1273 and 1277 cm^{-1} can also be identified in the figures. Additionally, the peaks at 1381 and 1385 cm^{-1} indicate that numerous NO_3^- free ions exist on the catalysts' surface, suggesting that gas may undergo surface ionization or that ammonium nitrate may become molten.

The catalyst was pretreated at $400\text{ }^\circ\text{C}$ with a flow rate of 40 mL/min in an argon atmosphere for 30 min . Subsequently, $500\text{ ppm NH}_3\text{-Ar}$ was introduced into the sample cell, and the IR spectra were recorded for 15 min . To remove the physically adsorbed NH_3 , the sample cell was purged with Ar for 10 min . After that, 500 ppm NO-Ar and $5\%\text{ O}_2$ were introduced into the cell for 30 min , during which time the IR spectra were continuously recorded. The resulting IR spectra of the two catalysts are plotted in Figure 8a,b. Another fresh catalyst was fitted into the sample cell, and it was first introduced into NO-Ar and O_2 for 15 min , followed by $\text{NH}_3\text{-Ar}$ for another 30 min . The resulting IR spectra of the two catalysts are plotted in Figure 8c,d.

2.10.1. NH_3 Passed over Pre-Adsorbed $\text{NO} + \text{O}_2$

Figure 9a,b show the IR spectra of the pre-adsorbed NO and O_2 of the 9n-Ce/SBA and 9n-Ce/SBA-S catalysts passed over by NH_3 . The adsorption of NH_3 on the catalyst is very different. In Figure 8a, the infrared absorption peaks of NH_3 adsorbed by Lewis acid are located at 3300 and 1338 cm^{-1} , respectively. However, in Figure 8b, after SO_2 treatment, the catalysts can function as a protic acid, specifically Bronsted acid, to adsorb NH_3 . Therefore, under the same scale, the adsorption strength of NH_3 in the 9n-Ce/SBA-S catalyst is much higher than that in the 9n-Ce/SBA catalyst. In addition, the nitrate intermediates on the catalyst are also different. The 9n-Ce/SBA catalyst has two types of intermediates, nitrite and monodentate nitrate. However, the 9n-Ce/SBA-S catalyst presents two types of free NO_3^- ions and NO_2^- salt, indicating that the intermediate on the 9n-Ce/SBA-S catalyst decomposes faster. This phenomenon is consistent with the improvement in $\text{NH}_3\text{-SCR}$ performance after sulfurization observed in some catalysts [21].

2.10.2. $\text{NO} + \text{O}_2$ Passed over Pre-Adsorbed NH_3

Figure 9c,d show the IR spectra of the pre-adsorbed NH_3 of the 9n-Ce/SBA and 9n-Ce/SBA-S catalysts passed over by NO and O_2 . The nitrate intermediates on the 9n-Ce/SBA-S catalyst are the same as those in Figure 8b, which are both NO_3^- and NO_2^- nitrites, indicating that the lattice oxygen of the catalyst is active and its surface is relatively smooth, which can allow NO_3^- to exist in the form of free ions. This may be related to the SO_2 poisoning of some CeO_2 active sites. In contrast, for 9n-Ce/SBA , there is only one intermediate, monodent nitrate, on the catalyst, indicating that the adsorption strength of NO in the catalyst is not high (which can be confirmed by comparing the height of the NO peak in the two figures), and it can also be inferred that the NO_2^- ion at 1277 cm^{-1} may be the IR peak of the nitro in ammonium nitrite. Furthermore, it is evident from the adsorption strength that a portion of NO is not adsorbed onto 9n-Ce/SBA , resulting in a higher proportion of reactions occurring on this catalyst according to the E-R mechanism compared to 9n-Ce/SBA-S . However, there are more nitrate species on 9n-Ce/SBA , which

indicates that this catalyst exhibits a strong adsorption capacity for NO. In conjunction with the rate equation presented in Section 2.8, it can be inferred that the dominant mechanism of the NH_3 -SCR reaction on the 9n-Ce/SBA catalyst is the Langmuir–Hinshelwood (L-H) mechanism, with a NO reaction order of 0.717.

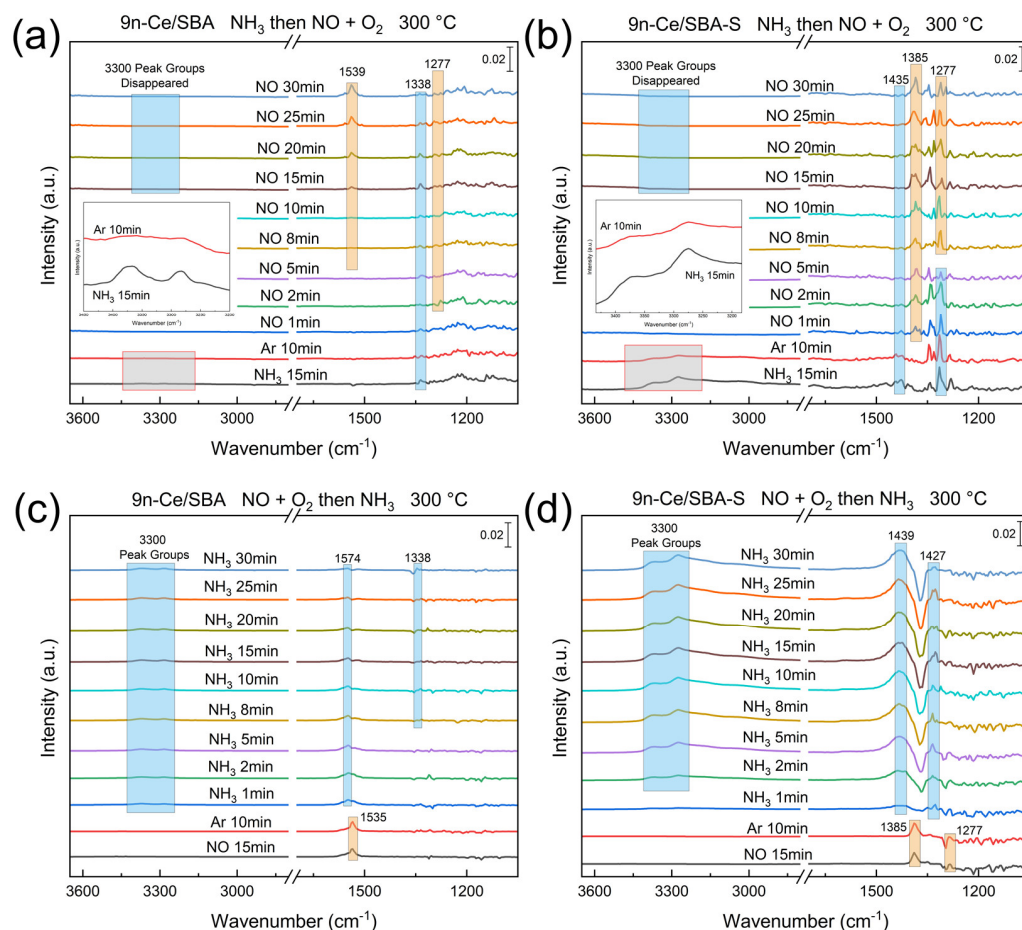


Figure 9. In situ DRIFT spectra of $\text{NO} + \text{O}_2$ adsorption with pre-adsorbed NH_3 at $300\text{ }^\circ\text{C}$ of (a) 9n-Ce/SBA, and (b) 9n-Ce/SBA-S and NH_3 adsorption with pre-adsorbed $\text{NO} + \text{O}_2$ at $300\text{ }^\circ\text{C}$ of (c) 9n-Ce/SBA and (d) 9n-Ce/SBA-S.

The mechanism of the reaction before and after poisoning is shown in Figure 10.

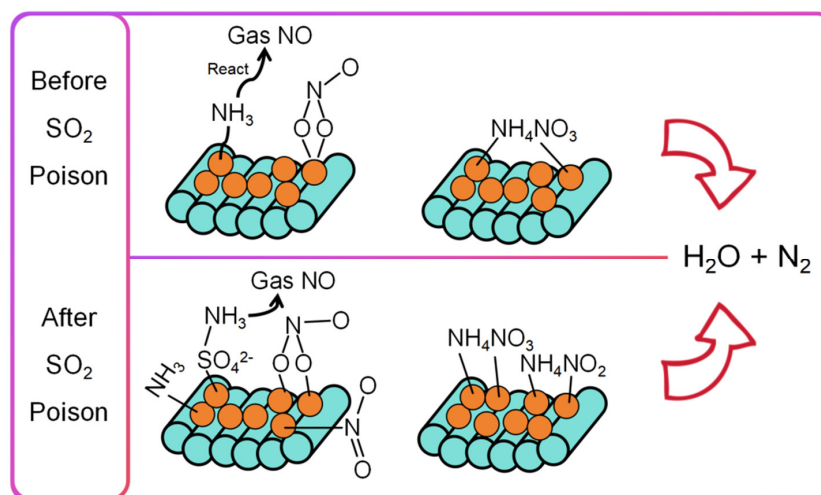


Figure 10. Schematic diagram of the reaction mechanism before and after SO_2 poisoning.

3. Materials and Methods

3.1. Catalyst Preparation

Preparation of Reagent. The following chemicals were used without further purification: $\text{Ce}(\text{NO}_3)_3 \cdot 6\text{H}_2\text{O}$ (99.5%, Rhawn, Shanghai, China), triethylamine (AdR, Macklin, Shanghai, China), polyvinylpyrrolidone (PVP K-30, Adamas, Shanghai, China), SBA-15 (pore size 6–11 nm, XFnano, Nanjing, China), and absolute ethanol (AR, Greagent, Shanghai, China).

Synthesis of CeO_2 nanospheres. The monodisperse nanospheres of CeO_2 were obtained by means of the hydrothermal method. Firstly, PVP (according to particle size) and 0.2 mmol $\text{Ce}(\text{NO}_3)_3 \cdot 6\text{H}_2\text{O}$ were dissolved with 20 mL ethanol, respectively. When the solutions in both beakers changed to clear, they were mixed together. Then, 0.415 mL triethylamine was slowly added dropwise to the above. After 10 min of stirring, the yellow solution was transferred into a 100 mL stainless-steel autoclave that was Teflon-lined. The sealed vessel was then heated at 180 °C for 24 h before it was cooled to room temperature. The CeO_2 nanospheres were dispersed into colloid homogeneously.

Loading nanospheres on SBA-15. A certain amount of CeO_2 colloid and SBA-15 were added into a crucible and heated at 70 °C until a gel appeared. Due to the well-developed pore structure of SBA-15 and the appropriate particle size range of the CeO_2 , most of the nanospheres entered the pore channels of the SBA-15 molecular sieves during the evaporation process. The gel was heated at 500 °C for 4 h with a rate of 5 °C/min in a muffle furnace. The powder obtained after cooling was the CeO_2 /SBA-15 catalysts (abbreviated as Ce/SBA). The different size of the particles was marked according to the D_{90} diameter and was given as X_n before Ce/SBA. The load percentage was indicated at the end using parentheses, but, for the catalysts with a 35% load, the load percentage was not be displayed. For example, 25%-loaded catalyst constituted of 7 nm nanospheres were marked as 7n-Ce/SBA(25%), while 35%-loaded catalyst comprising 5 nm nanospheres were marked as 5n-Ce/SBA. And the label of the 35%-loaded catalyst after having finished the SO_2 resistance test was achieved by adding *S* at the end of the name, such as 7n-Ce/SBA-S.

The catalyst synthesis process is shown in Scheme 1.



Scheme 1. Flow chart of the synthesis of the Ce/SBA series of catalysts.

3.2. Catalyst Characterization

Bruker (Billerica, MA, USA) D8 Advance is the instrument utilized for the X-ray diffraction (XRD) patterns of these catalysts. The target was Ni-filtered $\text{Cu K}\alpha$ radiation ($\lambda = 0.15418$ nm). The operating voltage was 40 kV, while the current was 40 mA. The diffraction intensity was collected and recorded when the diffraction angle moved from 5 to 80°.

The Thermo Fisher Nicolet iS50 FT-IR (Waltham, MA, USA) with an ATR infrared absorption detector for a solid substances spectrometer was the instrument utilized to perform the IR tests of the catalysts. The wavenumber range of the infrared light emitted by the transmitter was from 4000 to 500 cm^{-1} . The absorption data of each catalyst were collected 32 times. Moreover, the IR spectra in this work were published in the form of transmittance.

An FEI Talos F200x transmission electron microscope (TEM, Hillsboro, OR, USA) was used to shoot the images of the catalysts. The acceleration voltage was set to 200 kV. And the EDS mapping of the Ce, O, and other elements was obtained using EDS Super-X devices (Oxford Instruments, Abingdon, UK).

In addition to using TEM to calculate the particle size of the nanospheres, laser particle size gauges were also used to test the diameter of the nanospheres to obtain size data as realistic as possible. The particle sizes of the CeO₂ nanospheres were measured with Zetasizer Pro, a laser particle size analyzer manufactured by Malvern (Malvern, UK). A total of 1.5 mL of CeO₂ colloid was added into a cuvette with a 1 cm × 1 cm bottom; then, the cuvette was put into the particle size analyzer and tested in a closed environment at 25 °C.

The Micromeritics Autochem II 2920 chemisorption instrument (Micromeritics, Norcross, GA, USA) was used to perform NH₃ temperature-programmed desorption (NH₃-TPD) and H₂ temperature-programmed reduction (H₂-TPR). A thermal conductivity detector (TCD) (Tokyo, Japan) was used to detect the outlet gas concentration. In the NH₃-TPD test, about 100 mg of catalyst was fitted in a quartz tube. The sample was preprocessed at 100 °C in He for 30 min with a flow rate of 30 mL/min. Then, 10% NH₃-He was passed into the tube at 50 °C for 1 h. After 30 min of He purge (30 mL/min) to remove the physical adsorption of NH₃, the sample was heated from 50 to 500 °C at 10 °C/min in pure He to complete the desorption of NH₃, and data recording started. In the H₂-TPR test, about 200 mg of catalyst was also fitted in a quartz tube. The catalyst was preprocessed in Ar at 300 °C for 1 h with a flow rate of 30 mL/min, and then it was cooled to ambient temperature. After that, the H₂-TPR test temperature started from 50 to 800 °C at a rate of 10 °C/min with a gas flow of 5% H₂-Ar. H₂ consumption data and signal curves were recorded from 200 to 800 °C.

The Thermo Scientific K-Alpha XPS system (Waltham, MA, USA) was used as the instrument to perform the X-ray photoelectron spectroscopy (XPS) test on these catalysts. The excitation source was Al K α rays with an energy of 1486.6 eV. And a binding energy of C 1s = 284.80 eV was used to set charge correction.

Pore size data of the catalysts were calculated using the Barret-Joyner-Halenda (BJH) method. These data were obtained by N₂ isotherm adsorption and desorption tests on an ASAP2460 physical adsorption instrument made by Micromeritics (Norcross, GA, USA). The sample was degassed under vacuum at 250 °C for 4 h and a relative pressure range of P/P₀ = 0–1.0 during the test.

A sulfation rate test of the active components was carried on a fixed-bed reactor with an air flow path and a heater. The gas containing O₂ (5%), SO₂ (100 ppm), and N₂ in balanced proportions was passed into the reactor with the catalysts at 300 °C. The gas flow was 5000 mL/h, while the mass of the catalysts was 83 mg. Thermo Fisher's IGS Analyzer (Kandel, Germany) recorded the concentration of SO₂ over 1 h.

A thermogravimetric analysis (TGA) was performed on a NETZSCH STA 449 F3 synchronous thermal analyzer (NETZSCH, Beijing, China). A few milligrams of the catalyst were placed in the crucible, and the weight was recorded. The crucible was then heated from room temperature to 1300 °C in an argon atmosphere, and the weight curve of the catalyst and the heat absorption and release of the system were recorded.

In situ DRIFTS were collected at a wave number from 4000 to 650 cm⁻¹ via accumulating 32 scans on a Nicolet iS50 FT-IR spectrometer (Thermo Scientific, Waltham, MA, USA) fitted out with Harrick DRIFTS cell and a highly sensitive MCT detector cooled with liquid nitrogen. A total of 5 mg of the catalysts with KBr as substrate was filled into the sample compartment, and the gas content was the same as that of the NH₃-SCR performance test.

All of the test results were saved in the form of numerical values and drawn into curves using the OriginPro2023 software.

3.3. Catalytic Performance Measurements

NH₃-SCR performance test. A fixed-bed reactor with an air flow path and a heater was used as the catalyst performance test device. The gas used in the test contained NH₃ (500 ppm), NO (500 ppm), O₂ (5%), and N₂ in balanced proportions. The heater heated the temperature of the reactor from room temperature to 400 °C. The recording of the experimental data started at 200 °C and ended at 400 °C.

The gas containing NH₃ (500 ppm), NO (500 ppm), O₂ (5%), SO₂ (100 ppm), and N₂ in balanced proportions was passed into the fixed-bed reactor with the catalysts. The catalysts were heated to 300 °C and tested for their SCR performance for 1 h. Then, the heater maintained the temperature of the reactor at 300 °C, and the SO₂ gas flowed for 20 h. After turning off the SO₂ gas, the catalysts continued their performance testing for an additional 5 h.

In the above two tests, 83 mg of catalyst was fitted in a quartz tube of a 50 cm length and a 1 cm diameter, and the reactions were carried out at different temperatures with a space velocity of 60,000 mL/(g·h). The content of NO, NO₂, and N₂O of the outlet was detected using Thermo Fisher's IGS Analyzer (Kandel, Germany). All the results were saved as numerical data. And NO_x conversion was calculated with Equation (1), while N₂ selectivity was calculated using Equation (2):

$$\text{NO}_x \text{ conversion (\%)} = \left(1 - \frac{[\text{NO}]_{\text{out}} + [\text{NO}_2]_{\text{out}}}{[\text{NO}]_{\text{in}} + [\text{NO}_2]_{\text{in}}}\right) \times 100\% \quad (1)$$

$$\text{N}_2 \text{ selectivity (\%)} = \left(1 - \frac{2[\text{N}_2\text{O}]_{\text{out}}}{[\text{NO}_x]_{\text{in}} + [\text{NH}_3]_{\text{in}} - [\text{NO}_x]_{\text{out}} - [\text{NH}_3]_{\text{out}}}\right) \times 100\% \quad (2)$$

Reaction order test. A total of 8.3 mg of catalyst was fitted in a quartz tube 50 cm in length and 1 cm in diameter, and the reactions were carried out at different temperatures with a space velocity of 600,000 mL/(g·h). The catalyst was heated to 300 °C by varying the gas concentration to test the reaction order of the catalyst to the reactant; the rate equation was then established. Over the course of the test, the NO_x conversion was consistently below 25%. The form of the kinetic equation is shown in Equation (3). When testing the reaction order of NO, the NH₃ concentration was kept unchanged at 500 ppm, and the concentration of NO was increased from 0 to 1000 ppm. When testing the reaction order of NH₃, the concentration of NO was kept unchanged at 500 ppm, and the concentration of NH₃ was increased from 0 to 1000 ppm. However, when calculating the rate equation, an NH₃ concentration range of 400 to 1000 ppm was taken. When the O₂ reaction order was tested, the concentration of NO and NH₃ was kept constant at 500 ppm, and the O₂ concentration was increased from 1 to 5%.

$$r = -\frac{d[\text{NO}]}{dt} = k[\text{NO}]^x[\text{NH}_3]^y[\text{O}_2]^z \quad (3)$$

The reaction rate r was calculated using Equation (4):

$$r_i = \frac{c_{f,i} X_i V P_{\text{atm}}}{m_{\text{cata}} RT} \quad (4)$$

where m_{cata} is the mass of catalyst; $c_{f,i}$ is the concentration of substances i ; X_i is the NO_x conversion of the catalyst; V is the total flow rate; R is the molar gas constant; T is the room temperature; and P_{atm} is the standard atmospheric pressure.

4. Conclusions

In summary, CeO₂ nanospheres with different particle sizes were successfully synthesized and loaded onto an SBA-15 molecular sieve. During the NH₃-SCR test, the 9n-Ce/SBA catalyst with the largest size of nanospheres showed the best catalytic performance in the presence of 100 ppm SO₂, purifying over 90% of NO_x. To investigate the reason for its

superior SO₂ resistance, various characterization methods were used. The results of the NH₃-TPD showed that 9n-Ce/SBA has the most and strongest acid sites, while the H₂-TPR results indicated that this catalyst is hard to reduce below 450 °C. The XPS results proved that Si and Ce have a closer effect to stabilize the active center CeO₂. Based on these characterization results, it can be inferred that the superior SO₂ resistance of this catalyst is due to its low adsorption and oxidation of SO₂ to form sulfate. As a result, the amount of sulfate deposition on this catalyst's surface is the lowest, as confirmed by the TGA results. In situ DRIFTS revealed that, before and after poisoning, the NH₃-SCR reactions of the catalysts studied followed L-H and E-R mechanisms, but the proportion of reactions according to the L-H mechanism in 9n-Ce/SBA catalyst before poisoning was low.

Supplementary Materials: The following Supplementary Materials can be downloaded at <https://www.mdpi.com/article/10.3390/catal14020151/s1>, Figure S1: BJH pore distribution curves of pure SBA-15; Figure S2: Particle size distribution curves of different PVP addition amounts; Figure S3: NO_x conversion (a) and N₂ selectivity (b) curves of five different loading percentages of catalysts and pure CeO₂, (c) particle size distribution curves of PVP addition amounts of 7 mg/mL, and (d) NO_x conversion of 30n-Ce/SBA catalyst in 100 ppm SO₂ existing for 20 h; Figure S4: EDS mapping of Ce/SBA-S-series catalysts; Figure S5: (a) XPS spectrum of the Ce 3d orbital of 30n-Ce/SBA-S and (b) content of elements on the surface of 30n-Ce/SBA-S from XPS results; Figure S6: N₂ adsorption-desorption curve and pore distribution curve of some catalysts; Figure S7: Dependence of NO conversion rate upon (a) NO, (b) NH₃, and (c) O₂ concentrations; Figure S8: In situ DRIFT spectra of the adsorption of NH₃ at different temperatures of (a) 9n-Ce/SBA and (b) 9n-Ce/SBA-S; Figure S9: In situ DRIFT spectra of the adsorption of NO + O₂ at different temperatures of (a) 9n-Ce/SBA and (b) 9n-Ce/SBA-S; Figure S10: In situ DRIFT spectra of the reaction of NO, NH₃, and O₂ at different temperatures of (a) 9n-Ce/SBA and (b) 9n-Ce/SBA-S; Table S1: The amount of PVP added and the D₁₀, D₅₀, and D₉₀ size data obtained from the laser particle size analyzer; Table S2: The fitted NH₃-TPD data of the catalysts; Table S3: The fitted H₂-TPR data of the catalysts; Table S4: The binding energy of the peak U of the Ce 3d orbital of the catalysts after SO₂ poisoning; Table S5: Specific surface area, average pore volume, and pore size of the catalysts; Table S6: Materials corresponding to different wavenumbers and references. And the Supplementary Materials contain 6 references [9,34–38].

Author Contributions: Conceptualization, Y.Z. and K.L.; methodology, X.H. and M.B.; investigation, X.Y. (Xin Yang); resources, D.Z.; writing—original draft preparation, X.H.; writing—review and editing, Y.Z. and K.L.; supervision, X.Y. (Xiangguang Yang); funding acquisition, X.Y. (Xiangguang Yang), Y.Z. and K.L. All authors have read and agreed to the published version of the manuscript.

Funding: This research was funded by the National Natural Science Foundation of China (22072141, 22176185 and 52304429), the National Key Research and Development Program of China (2022YFB3504200, 2021YFB3501900), the Natural Science Foundation of the Jiangxi Province for Distinguished Young Scholars (20232ACB213004), the Jiangxi Provincial Key Research and Development Program (20232BBG70012), the Jiangxi Provincial Natural Science Foundation (20212BAB213032), the Youth Innovation Promotion Association of Chinese Academy of Sciences (2018263), the Jiangxi province's "Double Thousand Plan" (jxsq2020101047), and the Research Projects of the Ganjiang Innovation Academy, Chinese Academy of Sciences (E355C001 and E490C004).

Data Availability Statement: All data used in this study appear in the submitted article.

Conflicts of Interest: The authors declare no conflicts of interest.

References

1. Liu, M.; Shang, F.; Lu, X.; Huang, X.; Song, Y.; Liu, B.; Zhang, Q.; Liu, X.; Cao, J.; Xu, T.; et al. Unexpected response of nitrogen deposition to nitrogen oxide controls and implications for land carbon sink. *Nat. Commun.* **2022**, *13*, 3126. [CrossRef]
2. Wang, X.; Li, B.; Wang, Y.; Wei, T.; Li, S.; Li, W. Insight into the dynamic behaviors of reactants with temperature over a TiO_x-based catalyst for NO_x removal via NH₃-SCR. *Appl. Surf. Sci.* **2022**, *605*, 154689. [CrossRef]
3. An, X.; Feng, C.; Liu, J.; Cheng, G.; Du, Y.; Fan, Z.; Wu, X. Insight into the sulfur resistance of manganese oxide for NH₃-SCR: Perspective from the valence state distributions. *Appl. Surf. Sci.* **2022**, *592*, 153223. [CrossRef]
4. Zhao, W.; Rong, J.; Luo, W.; Long, L.; Yao, X. Enhancing the K-poisoning resistance of CeO₂-SnO₂ catalyst by hydrothermal method for NH₃-SCR reaction. *Appl. Surf. Sci.* **2022**, *579*, 152176. [CrossRef]

5. Vogt, E.T.C.; van Dillen, A.J.; Geus, J.W.; Janssen, F.J.G. Selective catalytic reduction of NO_x with NH₃ over a V₂O₅/TiO₂ on silica catalyst. *Catal. Today* **1988**, *2*, 569–579. [[CrossRef](#)]
6. Martín-Martínez, J.M.; Singoredjo, L.; Mittelmeijer-Hazeleger, M.; Kapteijn, F.; Moulijn, J.A. Selective catalytic reduction of NO with NH₃ over activated carbons. I: Effect of origin and activation procedure on activity. *Carbon* **1994**, *32*, 897–904. [[CrossRef](#)]
7. Kakuta, N.; Sugino, Y.; Rachi, H.; Ohkita, H.; Mizushima, T. Chemical removal of CeO₂ segregated on the surface of CeO₂-ZrO₂ binary oxides for improvement of OSC. *Top. Catal.* **2009**, *52*, 1888. [[CrossRef](#)]
8. Kakuta, N.; Morishima, N.; Kotobuki, M.; Iwase, T.; Mizushima, T.; Sato, Y.; Matsuura, S. Oxygen storage capacity (OSC) of aged Pt/CeO₂/Al₂O₃ catalysts: Roles of Pt and CeO₂ supported on Al₂O₃. *Appl. Surf. Sci.* **1997**, *121–122*, 408–412. [[CrossRef](#)]
9. Han, X.; Liu, K.; Bian, M.; Fang, Y.; Sun, J.; Zhang, Y.; Yang, X. CeO_{2-δ} nanoparticles supported on SnNb₂O₆ nanosheets for selective catalytic reduction of NO_x with NH₃. *ACS Appl. Nano Mater.* **2022**, *5*, 13529–13541. [[CrossRef](#)]
10. Li, X.; He, E.; Zhang, M.; Peijnenburg, W.J.G.M.; Liu, Y.; Song, L.; Cao, X.; Zhao, L.; Qiu, H. Interactions of CeO₂ nanoparticles with natural colloids and electrolytes impact their aggregation kinetics and colloidal stability. *J. Hazard. Mater.* **2020**, *386*, 121973. [[CrossRef](#)]
11. Zhang, X.M.; Zhang, Z.R.; Suo, J.S.; Ben, L.S. Synthesis of mesoporous silica molecular sieves via a novel templating scheme. *Chin. Chem. Lett.* **1999**, *129*, 23–30.
12. Shen, J.; Hess, C. Controlling the dispersion of ceria using nanoconfinement: Application to CeO₂/SBA-15 catalysts for NH₃-SCR. *Mater. Adv.* **2021**, *2*, 7400–7412. [[CrossRef](#)]
13. Zhang, L.; Li, L.; Cao, Y.; Yao, X.; Ge, C.; Gao, F.; Deng, Y.; Tang, C.; Dong, L. Getting insight into the influence of SO₂ on TiO₂/CeO₂ for the selective catalytic reduction of NO by NH₃. *Appl. Catal. B-Environ.* **2015**, *165*, 589–598. [[CrossRef](#)]
14. Zhu, J.; Ciolca, D.; Liu, L.; Parastaev, A.; Kosinov, N.; Hensen, E.J.M. Flame synthesis of Cu/ZnO-CeO₂ catalysts: Synergistic metal-support interactions promote CH₃OH selectivity in CO₂ hydrogenation. *ACS Catal.* **2021**, *11*, 4880–4892. [[CrossRef](#)] [[PubMed](#)]
15. Ma, K.; Guo, K.; Li, L.; Zou, W.; Dong, L. Cavity size dependent SO₂ resistance for NH₃-SCR of hollow structured CeO₂-TiO₂ catalysts. *Catal. Commun.* **2019**, *128*, 105719. [[CrossRef](#)]
16. Hu, X.; Chen, J.; Qu, W.; Liu, R.; Tang, X. Sulfur-resistant ceria-based low-temperature SCR catalysts with the non-bulk electronic states of ceria. *Environ. Sci. Technol.* **2021**, *55*, 5435–5441. [[CrossRef](#)]
17. Li, L.L.; Sun, B.W.; Sun, J.F.; Yu, S.H.; Ge, C.Y.; Tang, C.J.; Dong, L. Novel MnO_x-CeO₂ nanosphere catalyst for low-temperature NH₃-SCR. *Catal. Commun.* **2017**, *100*, 98–102. [[CrossRef](#)]
18. Chen, Y.; Chen, Y.; Hu, P.; Ma, S.; Li, Y. The effects of PVP surfactant in the direct and indirect hydrothermal synthesis processes of ceria nanostructures. *Ceram. Int.* **2016**, *42*, 18516–18520. [[CrossRef](#)]
19. Zhou, F.; Zhao, X.; Xu, H.; Yuan, C. CeO₂ spherical crystallites: Synthesis, formation mechanism, size control, and electrochemical property study. *J. Phys. Chem. C* **2007**, *111*, 1651–1657. [[CrossRef](#)]
20. Zhang, H.; Wang, W.; Zhang, B.; Li, H.; Zhang, Q. Controllable synthesis of spherical cerium oxide particles. *RSC Adv.* **2016**, *6*, 30956–30962. [[CrossRef](#)]
21. Xie, R.; Ma, L.; Li, Z.; Qu, Z.; Yan, N.; Li, J. Review of sulfur promotion effects on metal oxide catalysts for NO_x emission control. *ACS Catal.* **2021**, *11*, 13119–13139. [[CrossRef](#)]
22. Guo, K.; Ji, J.W.; Song, W.; Sun, J.F.; Tang, C.J.; Dong, L. Conquering ammonium bisulfate poison over low-temperature NH₃-SCR catalysts: A critical review. *Appl. Catal. B-Environ.* **2021**, *297*, 120388. [[CrossRef](#)]
23. Muzio, L.; Bogseth, S.; Himes, R.; Chien, Y.C.; Dunn-Rankin, D. Ammonium bisulfate formation and reduced load SCR operation. *Fuel* **2017**, *206*, 180–189. [[CrossRef](#)]
24. Zhang, W.J.; Liu, G.F.; Jiang, J.; Tan, Y.C.; Wang, Q.; Gong, C.H.; Shen, D.K.; Wu, C.F. Temperature sensitivity of the selective catalytic reduction (SCR) performance of Ce-TiO₂ in the presence of SO₂. *Chemosphere* **2020**, *243*, 125419. [[CrossRef](#)] [[PubMed](#)]
25. Zhang, L.; Zhao, Y.; Dai, H.; He, H.; Au, C.T. A comparative investigation on the properties of Cr-SBA-15 and CrO_x/SBA-15. *Catal. Today* **2008**, *131*, 42–54. [[CrossRef](#)]
26. Bae, Y.K.; Kim, T.-W.; Kim, J.-R.; Kim, Y.; Ha, K.-S.; Chae, H.-J. Enhanced SO₂ tolerance of V₂O₅-Sb₂O₃/TiO₂ catalyst for NO reduction with co-use of ammonia and liquid ammonium nitrate. *J. Ind. Eng. Chem.* **2021**, *96*, 277–283. [[CrossRef](#)]
27. Han, X.; Bian, M.; Liu, K.; Yang, X.; Zheng, D.; Yang, X.; Zhang, Y. Excellent MCM-49 Supported CeCuO_x nanocatalyst with ultrawide operating temperature window and strong anti-alkali ability for NH₃-SCR. *ChemNanoMat* **2023**, *9*, e202300407. [[CrossRef](#)]
28. Han, X.; Jin, S.; Rao, C.; Fang, Y.; Hu, B.; Liu, K.; Zhang, Y.; Yang, X. Mo-modified Pt/CeO₂ nanorods with high propane catalytic combustion activity: Comparison of phosphoric, sulphuric and molybdic acid modifications. *Mol. Catal.* **2023**, *548*, 113426. [[CrossRef](#)]
29. Xie, S.; Tan, W.; Li, Y.; Ma, L.; Ehrlich, S.N.; Deng, J.; Xu, P.; Gao, F.; Dong, L.; Liu, F. Copper single atom-triggered niobia-ceria catalyst for efficient low-temperature reduction of nitrogen oxides. *ACS Catal.* **2022**, *12*, 2441–2453. [[CrossRef](#)]
30. Maqbool, M.S.; Pullur, A.K.; Ha, H.P. Novel sulfation effect on low-temperature activity enhancement of CeO₂-added Sb-V₂O₅/TiO₂ catalyst for NH₃-SCR. *Appl. Catal. B-Environ.* **2014**, *152*, 28–37. [[CrossRef](#)]
31. Peng, Y.; Li, J.; Si, W.; Li, X.; Shi, W.; Luo, J.; Fu, J.; Crittenden, J.; Hao, J. Ceria promotion on the potassium resistance of MnO_x/TiO₂ SCR catalysts: An experimental and DFT study. *Chem. Eng. J.* **2015**, *269*, 44–50. [[CrossRef](#)]

32. Hu, W.; Zhang, Y.; Liu, S.; Zheng, C.; Gao, X.; Nova, I.; Tronconi, E. Improvement in activity and alkali resistance of a novel V-Ce(SO₄)₂/Ti catalyst for selective catalytic reduction of NO with NH₃. *Appl. Catal. B-Environ.* **2017**, *206*, 449–460. [[CrossRef](#)]
33. Wang, X.; Cong, Q.; Chen, L.; Shi, Y.; Shi, Y.; Li, S.; Li, W. The alkali resistance of CuNbTi catalyst for selective reduction of NO by NH₃: A comparative investigation with VWTi catalyst. *Appl. Catal. B-Environ.* **2019**, *246*, 166–179. [[CrossRef](#)]
34. Bian, M.; Liu, K.; Han, X.; Fang, Y.; Liu, Q.; Zhang, Y.; Yang, X. Novel manganese-based assembled nanocatalyst with “nitrous oxide filter” for efficient NH₃-SCR in wide low-temperature window: Optimization, design and mechanism. *Fuel* **2023**, *331*, 125857. [[CrossRef](#)]
35. Liu, J.; Shi, X.; Shan, Y.; Yan, Z.; He, H. Hydrothermal stability of CeO₂-WO₃-ZrO₂ mixed oxides for selective catalytic reduction of NO_x by NH₃. *Environ. Sci. Technol.* **2018**, *52*, 11769–11777. [[CrossRef](#)] [[PubMed](#)]
36. Qi, G.; Yang, R.T. Characterization and FT-IR studies of MnO_x-CeO₂ catalyst for low-temperature SCR of NO with NH₃. *J. Phys. Chem. B* **2004**, *108*, 4463–4469. [[CrossRef](#)]
37. Zhang, L.; Li, L.L.; Ge, C.Y.; Li, T.Z.; Li, C.J.; Li, S.X.; Xiong, F.; Dong, L. Promoting N₂ selectivity of CeMnO_x catalyst by supporting TiO₂ in NH₃-SCR reaction. *Ind. Eng. Chem. Res.* **2019**, *58*, 6325–6332. [[CrossRef](#)]
38. Hadjiivanov, K.I. Identification of neutral and charged N_xO_y surface species by IR spectroscopy. *Catal. Rev.* **2000**, *42*, 71–144. [[CrossRef](#)]

Disclaimer/Publisher’s Note: The statements, opinions and data contained in all publications are solely those of the individual author(s) and contributor(s) and not of MDPI and/or the editor(s). MDPI and/or the editor(s) disclaim responsibility for any injury to people or property resulting from any ideas, methods, instructions or products referred to in the content.